In situ neutron reflectometry reveals the interfacial microenvironment driving electrochemical ammonia synthesis

V.A. Niemann[1,2], M. Doucet[3]*, P. Benedek[1,2], N.H. Deissler[4], J.B.V. Mygind[4], S.W. Lee[1,2], I. Chorkendorff[4], A.C. Nielander[2]*, W.A. Tarpeh[1,2]*, T.F. Jaramillo[1,2]*

[1]Department of Chemical Engineering, Stanford University, Stanford, CA, USA.

[2]SUNCAT Center for Interface Science and Catalysis, SLAC National Accelerator Laboratory, Menlo Park, CA, USA.

[3]Neutron Scattering Division, Oak Ridge National Laboratory, Oak Ridge, TN, USA.

[4]Department of Physics, Technical University of Denmark, Kongens Lyngby, Denmark.

*doucetm@ornl.gov, anieland@slac.stanford.edu, wtarpeh@stanford.edu, jaramillo@stanford.edu

Abstract

Electrified interfaces are critical to the performance of energy systems and often demonstrate substantial complexity under operating conditions. Nanoscale understanding of the interfacial microenvironment, i.e., the solid electrolyte interphase (SEI), in lithium-mediated nitrogen reduction (Li-N_2R) is key for realizing efficient NH_3 production. Using in situ neutron reflectometry, we found the Li-N_2R SEI comprises a thick, diffuse outer layer and a thin, compact inner layer at low current cycling. Increasing current density resulted in a thinner outer layer with a thicker inner layer; sustained current led to LiH formation. Neutron absorption indicated boron uptake in the SEI. Time-resolved tracking of SEI growth with isotope contrasting revealed the proton donor modifies the inner layer, and the solvent modifies the outer layer. Li dendritic growth was observed in the absence of a proton donor. Our results inform Li-based systems and reaction microenvironments, and these methods can be applied broadly to interfacial energy technologies.

Introduction

Addressing challenges amidst climate change for sustainable water, food and energy supplies involves developing technologies that contain complex interfaces. These interfaces are difficult to interrogate under working conditions, and thus new methods have been developed to probe them under *in-situ* and *operando* conditions. Insights from these methods inform the rational design of interfaces for technologies spanning energy conversion,[1,2] water purification,[3] resource recovery,[4] energy storage,[1,2,5] and sustainable chemical production.[1,2,6] Of particular importance for energy storage and sustainable chemical production, *electrified* interfaces comprise an electrode and electrolyte undergoing dynamic changes that are not yet well understood.[7] In energy storage applications, electrified interfaces have been particularly important for lithium ion batteries (LIB) and lithium (Li)-metal batteries. LIBs operate outside the electrolyte stability window, leading to solid-electrolyte interphase (SEI) growth on the anode surface, and for Li-metal batteries, deposited Li reacts directly with the electrolyte to form the SEI. Controlling Li mobility and reactivity via SEI engineering is key to achieving high-capacity, long-cycling batteries.[5] Meanwhile, in sustainable chemical production, electrocatalysis features electrified interfaces comprising the electrode material and electrolyte double layer. These interfaces make up the "microenvironment" of the catalytic site and can modify kinetic, thermodynamic and mass transport aspects of chemical transformations. Accordingly, microenvironment engineering has been employed to enhance reaction selectivity, activity, and stability in electricity-driven transformations including H_2 evolution (HER),[1] CO_2 reduction to value-added products (CO_2R),[6] NO_3^- reduction to NH_3 (NO_3^-R),[8] O_2 evolution (OER),[1] and the focus of this work, N_2 reduction to NH_3 (N_2R).[9,10]

Often in energy storage and sustainable chemical production technology, the source, dynamics, and fate of protons within the interfaces are key determinants of performance. In the case of Li-metal batteries, the formation of dendritic lithium hydride (LiH) has been a major failure mechanism, and its detection and quantification remain a challenge.[11–13] Development of *in situ* and *operando* methods have made advancement in its detection in Li-base systems.[14] In electrocatalysis, proton transfer reactions at the electrolyte/electrocatalyst surface greatly impact reaction selectivity and rates.[15] In some cases, e.g., for titanium, nickel, and palladium cathodes, protons can intercalate into the electrode lattice, forming a hydride phase, which may play a role in reaction mechanisms and catalyst performance.[16]

The Li-mediated N_2 reduction to ammonia reaction (Li-N_2R) presents an opportunity for interfacial microenvironment engineering that involves unique proton dynamics. Li-N_2R is regarded as a reliable method for electrically-driven N_2 reduction to NH_3 at ambient conditions.[17] Developing ambient, electricity-driven alternatives to the Haber Bosch process would enable decentralized access to NH_3, the critical feedstock for fertilizer. Progress has been made in Li-N_2R to enable continuous NH_3 production

with long-term stability, although energy efficiency remains a challenge.[18,19] The mechanism of Li-N_2R can be broadly described in three steps: (1) Li is electrodeposited onto an electrode from an N_2-saturated electrolyte containing a lithium salt and proton donor.[20–22,17] (2) Li reacts with dissolved N_2 to form Li_3N.[23,24] (3) The proton donor, e.g., ethanol (EtOH), protonates Li_3N to form NH_3.[23,24] The electrodeposited Li also reacts with the solvent to form a solid-electrolyte interphase (SEI)[25] that governs N_2, Li^+, and H^+/proton donor transport to the Li surface. The proton donor can be incorporated into the SEI and can also form LiH, indicative of H_2 formation.[14,26,27] Based on previous work, we infer three pathways for proton-containing species: forming the SEI, producing the undesired species (e.g., H_2), and producing the desired species, NH_3.[28]

The Li-N_2R SEI is both a passivating layer for reactive Li and also serves to define the reaction microenvironment.[29] Early Li-N_2R studies utilized a $LiClO_4$-containing electrolyte,[17,20–22] and enhancements in selectivity were achieved with additives, e.g., O_2[10] and H_2O[30], and current cycling,[25] hypothesized to benefit the structure and composition of the SEI.[10,30] Due to the importance of the SEI, methods have been developed to understand and quantify its composition.[31] In situ methods include neutron reflectometry, which has been used to track the formation of the SEI while applying constant current density up to j = -0.5 mA/cm^2 for 2 minutes.[32] However, there is still a critical need to understand the nature of these interfaces at higher current densities and after passing more charge, consistent with the operational parameters expected to be needed for deployment. Advances in Li-N_2R performance have demonstrated enhanced selectivity and stability with the use of fluorinated salts, e.g., lithium tetrafluoroborate ($LiBF_4$) and lithium bis(trifluoromethanesulfonyl)imide (LiTFSI).[9,23] The enhanced performance has been attributed to the formation of a uniform, compact, stable SEI that includes LiF.[9,33] However, the presence of LiF is not the sole determinant of high performance, and more investigation is necessary to understand composition-structure-performance relationships.[29,34] Indeed, the $LiBF_4$ SEI layer has undergone study with ex-situ techniques, including X-ray photoelectron spectroscopy (XPS)[9,26] and cryo-transmission electron microscopy (cryo-EM)[26], which have revealed information post-experiment about possible morphology and speciation. The structure and composition of the SEI, however, is likely dynamic, and transient species may not be detectable post-experiment. Furthermore, delicate structures may be disrupted during sample preparation.[26,29] H- and Li-containing species can be particularly difficult to detect with benchtop, X-ray-based techniques. These limitations have motivated the development of *in situ* and *operando* techniques. A recent *operando* study used grazing-incidence wide-angle X-ray scattering (GIWAXS) to detect the presence of SEI species, including intermediates and LiH, and concluded that the enhanced performance of the $LiBF_4$ SEI was likely due to its ability to limit proton transport.[14] Key insights could be obtained using a technique that can track the location and longer-range structure of the SEI containing these species, with

sensitivity to LiH to understand the conditions under which it forms. Open questions remain as to how the structure and composition of the SEI change with current density and time; how the SEI forms; what the relative proton contributions of the proton-donor and solvent are; why $LiBF_4$ might perform better than other fluorinated salts; and how LiH, an indicator of major side product, H_2, forms.[29]

To answer these questions, we used neutron reflectometry to track current density dependence and time of applied current, SEI growth, and proton dynamics in $LiBF_4$-based Li-N_2R. The well-defined interfaces derived from the $LiBF_4$-containing electrolyte enabled detailed study of the system at higher currents and longer experiment times. Our time-resolved method enabled *in situ* tracking of SEI growth. Neutron sensitivity to light elements, including H and Li, enabled observation of the conditions leading to LiH formation[26,35–37] and tracking proton dynamics during SEI formation. We varied the deuteration of the proton donor, EtOH (EtOH), and solvent, tetrahydrofuran (THF), in dynamic and steady-state measurements to contrast proton- and Li-containing species. In all cases, layer thicknesses were determined – overcoming a challenge for ex situ techniques to date.[26,35] Finally, the unique property of boron for neutron absorption has indicated its presence in the SEI, suggesting a role with compositional benefits compared to other fluorinated salts. Our results inform the nanoscale design of SEIs, motivating the choice of additives and providing design rules for synthetic SEIs. Overall, this study provides methods and insights on energy materials involving interfaces and proton-containing species that can be applied to a wide range of applications at a critical moment in history for developing and adopting renewable technology.

Experimental

A complete description of materials and methods is found in the supporting information (SI). Briefly, the working electrode (WE) comprised a 5 nm titanium (Ti) sticking layer and 50 nm copper (Cu) layer deposited via physical vapor deposition (PVD) onto a 5 mm-thick silicon (Si) substrate. The counter electrode (CE) comprised 3 nm Ti and 100 nm platinum (Pt) deposited via PVD onto a 1 cm-thick Si substrate according to previous studies.[32,38] Typically, the electrolyte consisted of 1 M $LiBF_4$ in (d_8)-THF with 0.17 M (d_6)-EtOH and was saturated with N_2 gas. Delithiated lithium iron (II) phosphate ($Li_{0.5}FePO_4$) was used as a reference electrode.

Neutron reflectivity was measured at the Liquids Reflectometer (LR) at the Spallation Neutron Source, Oak Ridge National Laboratory.[39] The LR is a time-of-flight reflectometer with a neutron bandwidth of about 3.4 Å at an accelerator pulse rate of 60 Hz and about 6.8 Å at an accelerator pulse rate of 30 Hz. The wavelength range is from 2.5 Å to 17.0 Å, corresponding to a Q-range of $0.008 < Q < 0.21$

Å^{-1}. For this study, two measurements were utilized: "steady-state" measurements were conducted at 60 Hz across the full Q-range, meanwhile "dynamic" measurements were conducted at 30 Hz across a reduced Q-range for higher time resolution (bin size ~30-45 s).

The neutron reflectivity measurements were modeled using the Refl1d package as a set of slabs with varying scattering length density (SLD), thickness, and roughness, and parameter refinement was performed to determine the best fit.[40–42] A set of reference SLD values is found in Table S1.

Additional electrochemical tests were conducted in a custom-built, previously-reported glass cell[31,43] for air-free sample transfer to conduct scanning electron microscopy (SEM), X-ray photoelectron spectroscopy (XPS), and post-experiment rinsate analysis. The rinsate compositions were analyzed using inductively-coupled mass spectrometry (ICP-MS) and ion chromatography (IC).

Results & Discussion

Herein, we show the *in situ* formation and development of interfaces in Li-N_2R while varying current density, cycling vs. sustaining current, and deuteration of proton donor EtOH and solvent THF. Table 1 gives a summary of our experiments and results. First, **Experiment 1** examined changes in the SEI with increasing current density under current cycling and sustained current conditions. Before applying current (chronopotentiometry, CP), a steady-state reflectivity measurement was collected at 60 Hz across the full Q-range of $0.008 < Q < 0.21$ Å^{-1} to serve as a reference (time resolution ~ 45 mins). This measurement is shown in Figure 1a-b and labeled "Before CP." Later, we will show time-resolved data across a truncated Q range with 30 s time resolution. The Si substrate, a thin SiO_x layer, Ti sticking layer, and Cu layer of the WE are apparent in the SLD profile corresponding to the fitted model (Table S2). Subsequent steady-state measurements were taken at open-circuit after 2 minutes of applied current as shown in Figure 1a-b. Finally, j = -1.0 mA/cm^2 was held for approximately 1 hour, after which a steady-state measurement was collected at open circuit. The model values and calculated error are found in the SI (Tables S2-S8). Figure 1c shows the potential profiles corresponding to the cycling experiments, and the system set to open circuit potential (OCV) after each cycle for the 45 min steady-state measurements, and Figure 1d-f shows schematics corresponding to the results of the models.

125 **Table 1:** Summary of experiments, model parameters, and key results

Experiment / electrolyte	Electrochemistry/current density (j)	Neutron measurement	Inner / Outer SEI	Model Parameters		
				SLD (10^{-6}/Å^2)	Thickness (Å)	Roughness (Å)
1. d_8-THF 0.17 M EtOH 1 M $LiBF_4$	**Low current cycling (2 mins):** -0.5 mA/cm^2 -0.5 mA/cm^2 -1.0 mA/cm^2	Steady-state between cycles @ OCV	Inner	1.6-1.9	42-44	7-12
			Outer	2.3-2.5	222-230	66-75
	High current cycling (2 mins): -2.0 mA/cm^2 -3.0 mA/cm^2	Steady-state between cycles @ OCV	Inner	2.3-2.4	151-164	53-57
			Outer	-0.6-0.5	99-125	99-100
	Sustained current (68 mins): -1.0 mA/cm^2	Steady-state between cycles @ OCV	Inner	1.0	111	57
			Outer	-2.7	155	87
	Results: *Low current cycling* experiments show a thin, compact inner and rough outer layer. *High current cycling* experiments show an inner layer with a higher SLD that is thicker and rougher; outer layer is thinner and rougher. The *sustained current* experiment shows lowest SLDs of the inner and outer layers. (Figure 1).					
2. d_8-THF 0 M EtOH, 1 M $LiBF_4$	-0.3 mA/cm^2 for 5 mins	Time-resolved; Steady-state @ OCV	Inner	2.8	89	13
			Outer	3.2	257	79
	-0.3 mA/cm^2 for 12 mins	Steady-state @ OCV	Inner	2.5	92	25
			Outer	3.0	272	78
	-0.3 mA/cm^2 for 30 mins	Steady-state @ OCV	Layer	2.7	363	77
	Results: Distinct layers combine to form 1 main layer at an average SLD of 2.7. Likely accumulation of Li dendrites based on supporting experiments using matching electrolyte and electrochemical tests. (Figure 2and 3)					
3. d_8-THF 0.17 M EtOH 1 M $LiBF_4$	-0.3 mA/cm^2 for 4 mins	Time-resolved; Steady-state @ OCV	Inner	0.3	32	17
			Outer	4.4	174	59
	-0.3 mA/cm^2 for 12 mins	Steady-state @ OCV	Inner	0.1	27	22
			Outer	4.4	179	56
	-0.3 mA/cm^2 for 30 mins	Steady-state @ OCV	Inner	-0.8	26	22
			Outer	4.4	179	70
	Results: The inner layer has the most negative SLD of the electrolyte conditions at -0.3 mA/cm^2. The inner layer is an order of magnitude thinner than the 0 vol% EtOH condition. (Figure 2/3)					
4. d_8-THF 0.17 M d_6-EtOH 1 M $LiBF_4$	-0.3 mA/cm^2 for 4 mins	Time-resolved; Steady-state @ OCV	Inner	3.6	40	14
			Outer	3.9	182	56
	-0.3 mA/cm^2 for 12 mins	Steady-state @ OCV	Inner	3.2	25	17
			Outer	3.8	208	75
	-0.3 mA/cm^2 for 30 mins	Steady-state @ OCV	Inner	3.5	41	6
			Outer	3.8	206	71
	Results: The inner SLD is significantly higher than that of the non-deuterated EtOH experiment, and the inner layer has similar thickness. (Figure 2 and3)					
5. THF 0.17 M d_6-EtOH 1 M $LiBF_4$	-0.3 mA/cm^2 for 4 mins	Steady-state @ OCV	Layer	1.6	79	35
	-0.3 mA/cm^2 for 12 mins	Steady-state @ OCV	Inner	3.3	53	35
			Outer	1.6	149	61
	-0.3 mA/cm^2 for 30 mins	Steady-state @ OCV	Inner	3.7	47	31
			Outer	1.9	129	75
	Results: Outer layer SLD is affected by the deuteration of the solvent, bringing it to lower SLDs. (Figure 3)					

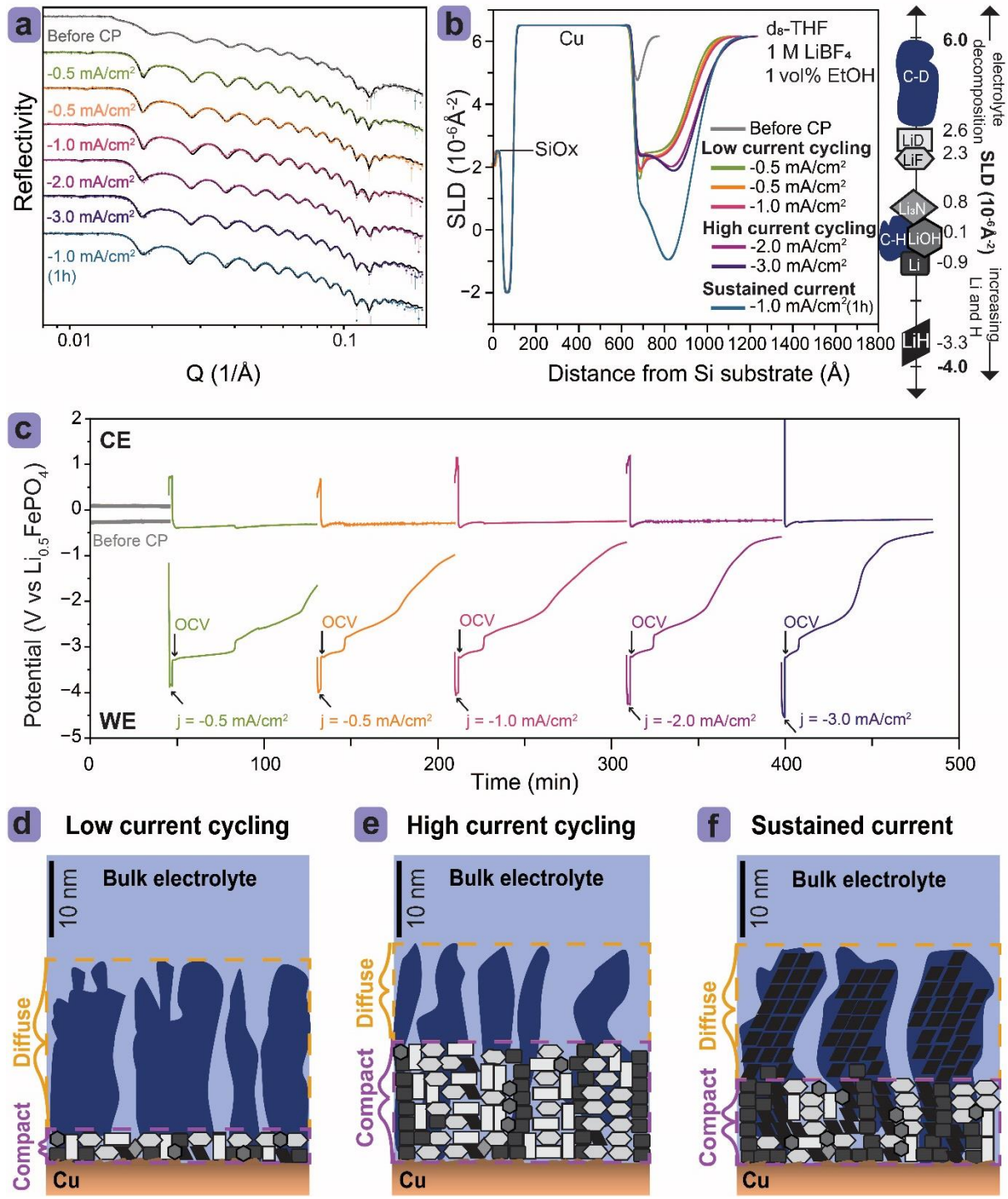

Figure 1. *(a) Steady-state reflectivity measurement (points) and model fits (solid lines). (b) model SLD profiles corresponding to each steady state measurement. (c) electrode (WE) and counter electrode (CE) potentials for each cycle. Open circuit was held after each cycle to allow for a steady-state measurement. (d-e) Schematic of inner and outer layers during (d) low current (j = -0.5 to -1.0 mA/cm²) and (e) high current (j = -2.0 to -3.0 mA/cm²) cycling. (f) sustained current (j = -1.0 mA/cm² for 68 minutes) schematic of inner and outer layers. Potential profiles for the sustained current experiment can be found in Figure S1.*

$LiBF_4$ forms well-defined interfaces at higher current and more charge passed than $LiClO_4$

Our results show the formation of a Li-containing, *inner layer* and a porous, *outer layer* after applying j = -0.5 mA/cm^2 for 2 mins (Figure 1). Upon applying another j = -0.5 mA/cm^2 for 2 mins, the inner and outer layers retained a similar structure (Figure 1b), and the OCV potentials took over an hour to approach pre-CP values. Increasing current density to j = -1.0 mA/cm^2 resulted in similar structures and compositions of interfaces. Subsequent high current cycling (j = -2.0, -3.0 mA/cm^2) and sustained current experiments (j = -1.0 mA/cm^2; 68 min) were achievable with $LiBF_4$. These results indicate that well-defined, stable SEI structures were achieved with $LiBF_4$ in contrast to previous measurements made with a $LiClO_4$-based electrolyte, indicating that the $LiBF_4$-derived SEI layer is more effective at limiting Li reaction with the electrolyte.[32] We also do not observe the full dissolution/pore filling of the outer layer that has been previously observed in the $LiClO_4$-based system.[32] More generally, Li-battery SEIs, including those derived from $LiBF_4$ dissolved in THF,[44,45] have been determined to comprise an inner inorganic layer and an outer organic layer.[44–46] We maintain the same terminology with the distinction that the Li-N_2R inner layer also incorporates the plated Li. We note previous Li-N_2R work has utilized "impermeable" and "permeable" SEI components, respectively.[47,48] The inner layer SLD does not match the SLD of Li, but it likely contains Li along with other Li-containing species based on its value of ~1.5 10^{-6}/Å^2 — this value is substantially lower than the electrolyte background of ~6.2 10^{-6}/Å^2 and is consistent with a combination of majority species, Li (-0.88 10^{-6}/Å^2) and LiF (2.30 10^{-6}/Å^2) and possible minority species Li_3N (0.80 10^{-6}/Å^2) and LiH (-3.33 10^{-6}/Å^2) (Figure 1b; Table S1). While the presence of EtOH can lead to a disordered interfacial morphology, and small amounts of inorganics may distribute through the outer layer, our results show that on average, our inner and outer layers have distinct compositions.[26,48]

Increasing current leads to electrolyte degradation in inner layer and less effective reactant screening by outer layer

Compositional differences are evident in inner and outer layers between the low current cycling profiles (j = -0.5 mA/cm^2, -1.0 mA/cm^2) to the high current cycling profiles (j = -2.0 mA/cm^2, -3.0 mA/cm^2). We grouped low vs. high based on compositional and morphological characteristics of the SLD profiles. The high current cycling inner layers have a higher SLD than the low current cycling inner layers. These values match closely but exceed the LiF SLD of (2.30 10^{-6}/Å^2), consistent with the presence of d_8-THF degradation products including LiD (2.84 10^{-6}/Å^2), poly-d_x-THF and some pore filling of d_8-THF. The change of the inner layer composition resulting from an increase in current density aligns with previous studies on battery interfaces where increased lithiation can induce strain on the inorganic portion of the SEI, causing it to crack, exposing fresh Li to react further with the electrolyte, thus producing electrolyte

decomposition species.[14,49,50] Cracking could explain the transition from a lithiated inner layer to an inner layer comprised of electrolyte decomposition as current density increases.

The low current cycling inner layer is thinner and less rough than the high current cycling inner layer, suggesting that operating at low current cycling could inhibit SEI cracking, whereas high current density cycling could lead to SEI cracking and dendritic growth.[48] In a previous Li-N_2R study using $LiBF_4$, current density effects have been attributed to N_2 transport limitations as opposed to differences in reactivity based on Li morphology,[23] however Li morphology may result in a different structure and composition of the SEI, affecting N_2 transport, thereby affecting NH_3 selectivity.

Meanwhile, the low current cycling outer layer has SLD values ~2.3 $10^{-6}/Å^2$ (Figure 1b) matching well with LiF (2.30 $10^{-6}/Å^2$). The high current cycling outer layer SLD values ~1.7 $10^{-6}/Å^2$ (Figure 1b) are lower than those of the low current cycling layers. These values correspond to more Li- and H-containing species, e.g., Li (-0.88 $10^{-6}/Å^2$), lithium ethoxide (LiEtO) (-0.16 $10^{-6}/Å^2$) and LiH (-3.33 $10^{-6}/Å^2$). The roughness value of up to 75 Å for this layer could indicate that it is a porous layer containing organics derived from the proton-donor and d_8-THF. Previous reports demonstrated that the proton donor has a direct impact on the structure and composition of the organic portion of the SEI, positing that it can serve as an inhibitor to species transport.[31,47,51] In the case of compositional differences in the outer layer, we hypothesize that a crack initiated in the inner layer could give rise to reactions of electrolyte species and drive the formation of lithiated and non-deuterated (proton-containing) degradation products in the outer layer.[49]

The low current cycling outer layer is thicker but less rough than its high current counterpart, likely resulting in better Li passivation. The high current cycling outer layer, however, has a significantly lower SLD, likely due to incorporation of Li-and H-containing species. Inner layer cracking at high current cycling could facilitate Li reaction with EtOH to form LiH, and it is possible that more dendritic SEI layers form. Additionally, a possible SEI species is LiEtO, which would contribute to a negative SLD with its presence in the layer and has previously been shown to be incorporated into the SEI.[22, 93] The outer layer is thinner but also rougher after the high current cycling experiments, indicating a less controlled growth and larger pores, which could enable more transport of side reactants, i.e., EtOH and d_8-THF degradation products, to the Li layer.[47] Previous work described the effect of proton donor concentration on NH_3 selectivity by describing the permeability of the SEI, suggesting a tradeoff between low permeability, i.e., N_2 diffusion limitations through the layer, and high permeability, where proton donor diffusion leads to adverse side reactions, i.e., H_2 production.[47] While this model did not describe current density effects on SEI permeability, it does give context for the results presented here, where higher current densities lead to

rougher, thinner outer layers, permitting the proton donor and THF degradation products to diffuse to react with the Li surface.

Sustained current leads to the accumulation of LiH

Next, sustained current at j = -1.0 mA/cm^2 for 68 minutes was measured (potential profiles shown in Figure S1), and separate bench top experiments were conducted at the same current density to measure NH_3 production in the same neutron cell (Figure S2, Table S9). The resulting SLDs of the inner and outer layers were significantly lower than the SLD values of low current cycling. These more negative values correspond to the increased presence of Li- and H-containing species. In the case of the outer layer, the SLD profile (Figure 1b) decreases to an SLD of ~-1.0 10^{-6}/Å^2 (Figure 1b), far lower than the SLD of previous experiments, indicating the occurrence of a species with a strongly negative SLD. The species most likely to shift the SLD in this drastic manner is LiH at -3.33 10^{-6}/Å^2 (Figure 1b). To explain this LiH formation, one hypothesis is that Li plating could result in tensile stress on the inorganic, inner layer, leading to cracking. The freshly plated Li could then be exposed to proton donor EtOH and H_2 generated at the cathode. The Li and H-containing species would then react to form LiH, indicative of the side reaction pathway towards H_2, which has previously been theoretically predicted to form but difficult to observe ex situ.[26,51] Recently, it has been detected *in operando,*[14] and our results show the conditions that favor its formation and growth into the outer SEI.

Structurally, the sustained current inner layer has a higher thickness and roughness at its interface with the outer layer than the low current cycling layers (Table S8). Interestingly, the outer layer of the sustained current experiment (155 Å) is thinner than that of the low current cycling layer (222-230 Å) (Table 1). The smaller thickness and greater roughness could result in less screening of side reactants, and together with increased availability of H^+, side product pathways (LiH) become favored over the Li_3N pathway towards NH_3. These findings further justify the benefits of cycling on controlling Li reactivity.[25,32]

***In situ* detection of boron-containing species in the SEI**

We also observed neutron absorption dips under the critical edge of the steady state reflectivity measurements, indicative of boron-incorporation into the SEI (Figure S3). For models of reflectivity curves after applying current, the best fits incorporate this absorption term (Tables S3-8). It is possible that some B-containing species form the reported Li_xBF_y.[52,53] BF_4^- may also decompose into LiF and BF_3, and that the BF_3 reacts with organics to form part of the porous, outer layer, which has been hypothesized.[14,52,54] The presence of boron in the SEI could confer beneficial structural and compositional properties for Li-N_2R, which will be the focus of future work.[9,35,53,54]

Because this method is *in situ*, we are studying the interfaces in their native, electrochemical environment.[55] Neutron irradiation of the electrolyte causes residual radioactivity post-experiment, posing safety concerns for post-experiment NH_3 product analysis to determine performance metrics and make the step from *in situ* to *operando*. This limitation is aided by parallel bench-top experiments for electrolyte analysis and electrode characterization. To make the step to *operando* measurements, one must develop analytical methods to safely detect irradiated products at the neutron beam line. Our work to date shows the fundamental understanding that becomes accessible with method development, and further advancement will deepen our understanding of electrified interfaces.

Dynamic measurements of early SEI growth show the proton donor influences the inner layer composition and the solvent influences the outer layer composition

We used time-resolved neutron reflectivity measurements to track SEI formation at j = -0.3 mA/cm^2, the lower limit reported for $LiBF_4$-based Li-N_2R,[23] to capture changes on a relevant and method-compatible time scale. These measurements included a proton donor/solvent deuteration contrast series listed as **Experiments 2-4** in Table 1. The results are shown in Figure 2a-f, and tabulated model parameters for the fits are given in Tables S10-15.

First, we focus on common electrochemical behavior between the experiments. For the first 80 seconds of CP, the WE potential reaches a plateau at -2 V vs $Li_{0.5}FePO_4$ before reaching Li plating potential (Figure 2a, c, e). This potential profile behavior is consistent with the current understanding of SEI formation, which starts at an intermediate potential between open circuit potential (OCV) and Li plating.[45] During this potential plateau, we see the most marked changes in the SLD profiles from the initial state for all conditions (Figure 2b, d, f). Specifically, the SLD profiles show the emergence of an inner layer with a lower SLD than the initial conditions and electrolyte background, followed by an outer layer that approaches the value of the electrolyte background. We note that in cases with EtOH (Figure 2c,e), a reduction peak between -2 and -3 V vs $Li_{0.5}FePO_4$ has been previously observed and attributed to H_2 production from EtOH-derived protons.[51] Our time-resolved measurements indicate that this H_2 production happens concurrently with SEI formation (Figure 2d, f).

Figure 2b shows the formation of inner and outer layers using a d_8-THF based electrolyte in the absence of EtOH. Model parameters indicate a thickness of approximately ~25 nm of the outer layer, in agreement with a previous ex-situ cryo-electron microscopy study.[26] The majority of changes to the SLD profile correspond to the first ~100 seconds of CP, where there is a potential plateau at -2.0 V vs. $Li_{0.5}FePO_4$.

Qualitatively, the inner layer in d_8-THF, no EtOH is thicker than the inner layers formed in the presence of EtOH (Figure 2d,f). The d_8-THF, no EtOH inner layer growth is accompanied by the growth of the outer layer after the potential plateau and during Li plating (Figure 2a-b), resulting in a single, thick layer. This is consistent with the hypothesis that the absence of EtOH enables the accumulation of Li and inner layer Li species (Figure 2a-b).

Comparing the d_8-THF, EtOH and d_8-THF, d_6-EtOH experiments, we observe that most changes are also occurring at the potential plateau between -2 and -3 V vs $Li_{0.5}FePO_4$. The SLD of the d_8-THF, EtOH inner layer is the lowest of the inner layers at 0.28 $10^{-6}/Å^2$, indicating that protons from the EtOH play a role in defining the inner layer composition (Figure 2d). The thicknesses of the inner layer in both d_8-THF, EtOH and d_8-THF, d_6-EtOH experiments are much smaller than the d_8-THF, no EtOH experiment, and remain constant after SEI formation, indicating that Li reacts at a similar rate as it is plated in the presence of EtOH. The inner layer is still always apparent, consistent with findings from literature that it is a relatively stable Li-containing layer that does not significantly grow after 1 minute of CP.[47,51] These results are consistent with the understanding that EtOH modifies SEI composition and morphology but also reacts with deposited Li.[26,31,51,56] Meanwhile, some variations in the SLD in the outer layer could result from the disordered nature of disrupted SEI formation due to the presence of EtOH.[26] As far as the composition of the outer layer, it could comprise THF degradation products resulting from ring-opening reactions as previously observed.[32,57,58] Some contributions may come from lithium ethoxide, previously observed in the $LiClO_4$-based SEI,[31] and it has been inferred in a $LiBF_4$-based system using *ex situ* XPS[26] and identified in an *operando* GIWAXS study.[14]

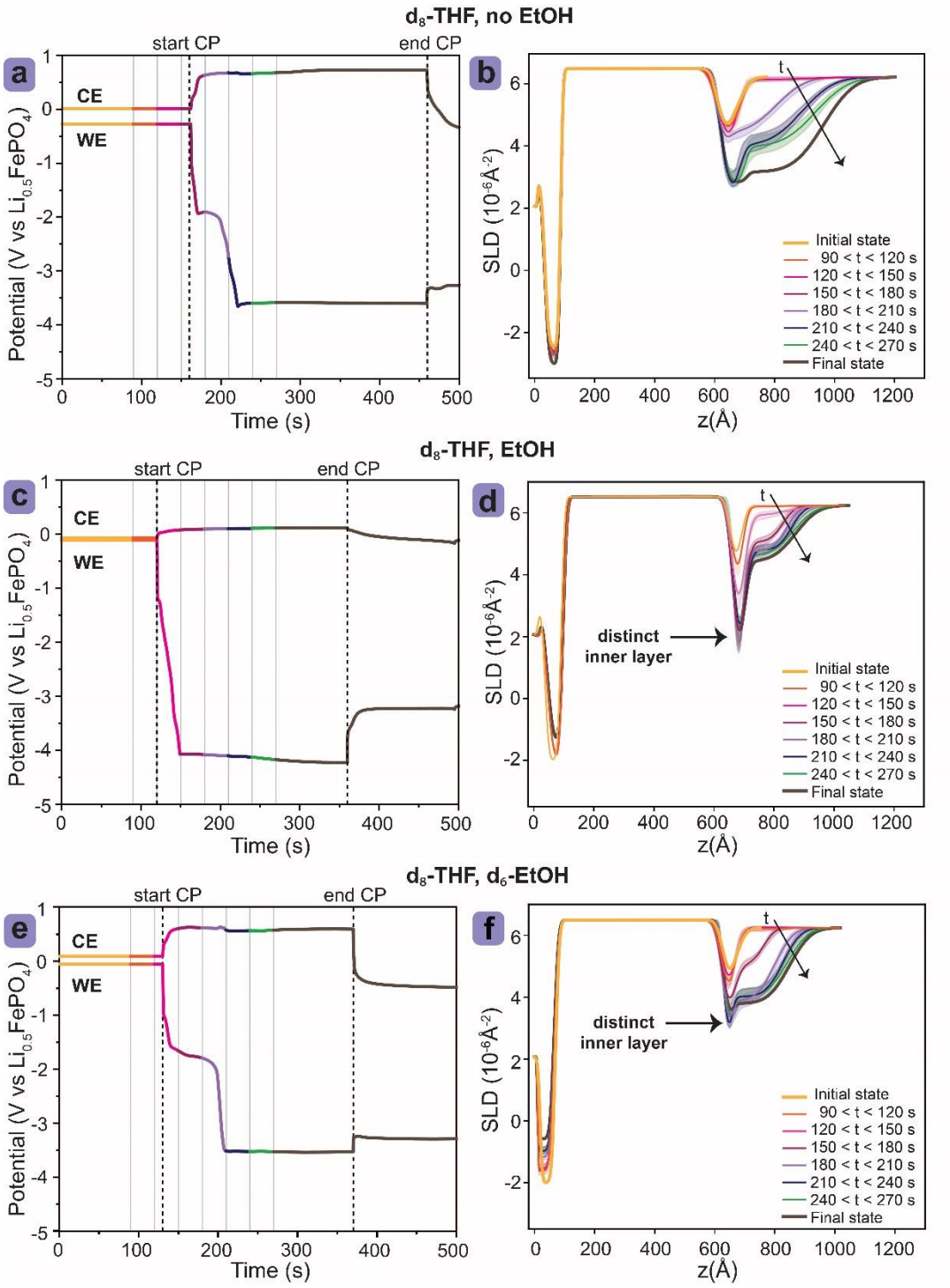

279

280 ***Figure 2.*** *Time-resolved potential (left) and SLD profiles (right) during Li-N_2R reaction (a-b) without*
281 *EtOH, (c-d) with non-deuterated EtOH and deuterated THF, and (e-f) with deuterated EtOH and deuterated*
282 *THF. Time-resolved fit error is shown in shaded regions about the solid-line fit. Note, the electrolytes were*
283 *pre-saturated with N_2 in all cases.*

Steady-state measurements of SEI show the accumulation of Li without EtOH and longer-term proton contributions of proton donor versus solvent

Figure 3a-c shows the steady-state measurements after an experiment comprising 3 cycles of applied constant current at j = -0.3 mA/cm^2. Added to the set of experiments described in Figure 2 is the case where the solvent is non-deuterated THF with d_6-EtOH labeled **Experiment 5** in Table 1. The steady-state reflectivity model parameters are given in Tables S16-25 and the potential profiles are given in Figures S5. Contrast between H and D, where H contributes a negative SLD value, and D contributes a positive SLD value, indicates which electrolyte species serve as the H/D source during SEI growth.

In the absence of EtOH (**Experiment 2** in Table 1), Li is plated into a dendritic morphology. The same electrochemical conditions applied to a Cu foil in a glass cell (See Figure S6 and Table S26) verify the presence of dendrites in SEM images obtained with air-free sample transfer (Figure S7), agreeing with previous work.[26] The lower inner layer SLD around 3 x 10^{-6}/Å^2 is likely a weighted average of d_6-THF degradation products, Li, and LiF, where Li and LiF have been detected after the analogous experiment in a glass cell (Figure S11a, c). By the end of the third cycle in Figure 3c, the best-fit reflectivity models have just one material layer on the working electrode surface after ~47 mins of CP, indicating dendrite growth.

When comparing the SLDs of the inner layers for the EtOH experiments, we see that the identity of the proton donor, i.e., whether it is deuterated, most affects the SLD. In the d_8-THF, EtOH experiment, the inner layer has the lowest SLD consistently after each cycle, with model SLD inputs of 0.3 10^{-6}/Å^2, 0.1 10^{-6}/Å^2, and -0.8 10^{-6}/Å^2 after the first, second, and third cycles, respectively (Tables S13, S20, S21). We can compare these inner layer SLD values to those of the experiments using d_6-EtOH. In the d_8-THF, d_6-EtOH case, listed in Table 1 as **Experiment 5**, the model SLD inputs are 3.6, 3.2, and 3.4 10^{-6}/Å^2 (Tables S15, S22, S23). The inner layer SLDs are similar for the THF, d_6-EtOH experiment after the second and third cycles: 3.3 and 3.7 10^{-6}/Å^2 (Tables S24, S25). We compare the model inputs for clarity, but it is also apparent from the SLD profiles, especially after cycle 3 (Figure 3c) that the inner layer composition is most drastically impacted by the presence and identity of the proton donor. These results indicate that the proton donor likely reacts with the Li-containing, inner layer to contribute H-containing species to that layer, including LiH.

Meanwhile, when comparing the SLDs of the outer layers formed in the presence of EtOH, we see that the deuteration of THF affects the outer layer SLD. The outer layers range from 3-5 10^{-6}/Å^2 for the d_8-THF experiments, with both d_6-EtOH and EtOH, meanwhile the outer layer for non-deuterated THF ranges from 1.59 to 1.88 x 10^{-6}/Å^2. SEM images of a Cu foil from an equivalent glass cell experiment show porous layers formed in the cases with EtOH (Figure S8). As a result, the major component of the outer, organic

layers would be THF degradation products and pore-filling of the electrolyte. In the current case, the outer layer is still distinguishable from the background electrolyte; the filling of its pores could enable the transfer of protons from either proton donor or electrolyte decomposition products to the Li-containing layer.[56]

When comparing morphology, the experiments with EtOH have similar thicknesses in inner and outer layers. Meanwhile, the experiments without EtOH exhibit a thicker inner layer that dominates over the outer layer, such that the associated SLD profile in Figure 3c shows one, rough layer on top of the Cu working electrode. This result demonstrates the accumulation of electroplated Li in the absence of EtOH, and its roughness together with air-free transferred SEM images of matching experiments in a glass cell indicate the formation and growth of Li dendrites (Figure S7).

As previously mentioned, the same electrochemical tests were applied to a Cu foil working electrode in a glass cell, sparging nitrogen in an Ar environment (potential profiles and experimental results presented in Figures S6a-b and Table S26). The dimensions of the Cu foil (1 cm x 1 cm) enabled the use of a transfer vessel to image the electrodes via SEM (Figures S7-8) and measure XPS (Figures S9-12) with minimal exposure to air. These dimensions also enabled analysis of the electrode rinsate via ICP-MS and ion chromatography, (Tables S27-30, Figures S13-14,). The XPS and electrode rinsate studies verified the presence of SEI components including LiF and boron-containing species.

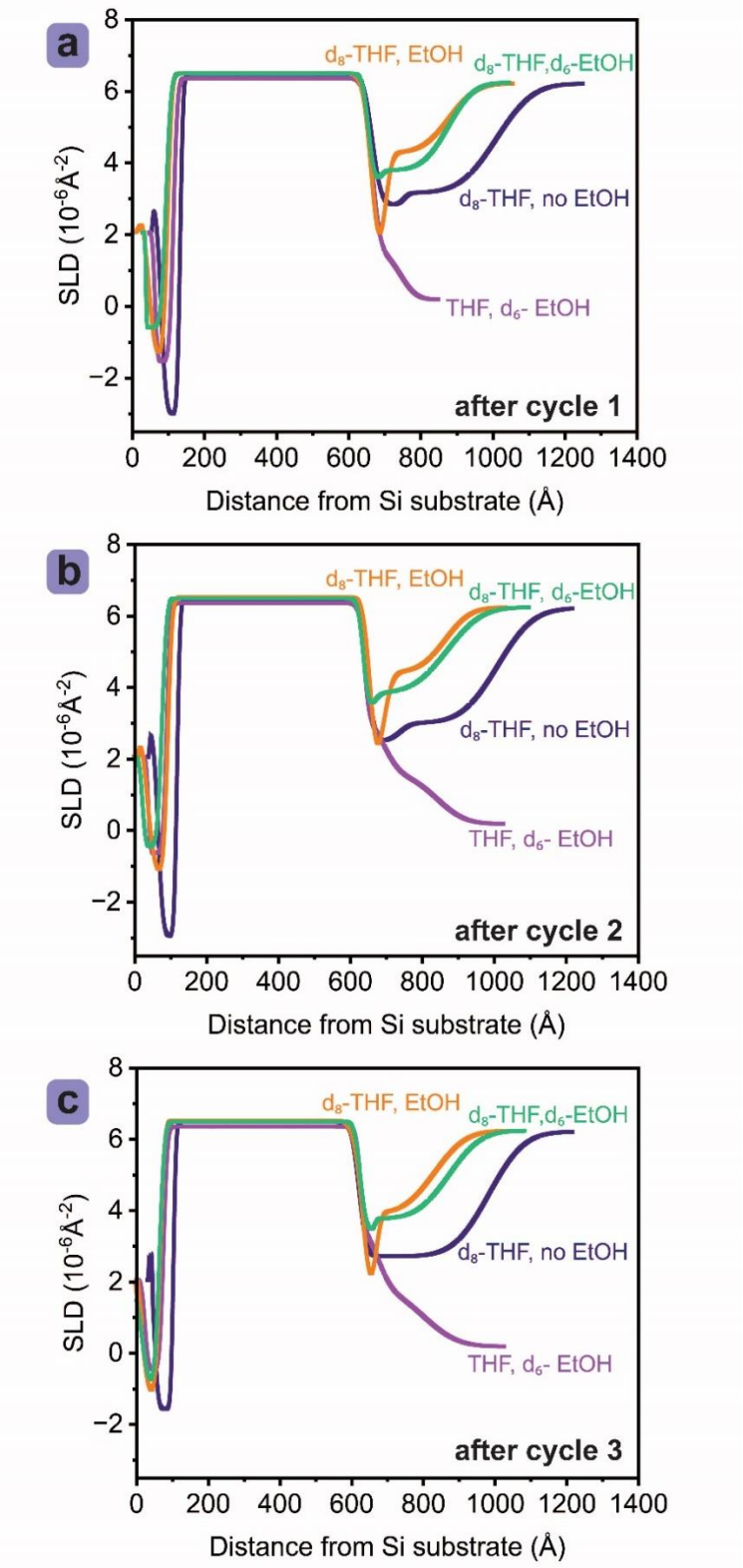

342 ***Figure 3***. *(a) Steady state SLD profiles after the first cycle at j = -0.3 mA/cm^2 lasting 4-5 min. (b) Steady-*
343 *state SLD profiles after the second cycle at j = -0.3 mA/cm^2 lasting 12 min. (c) Steady state SLD profiles*
344 *after the third cycle at j = -0.3 mA/cm^2 lasting 30 min.*

Contextualizing neutron reflectometry results with previous Li-N_2R research

Figure 4 graphically summarizes our findings with respect to current understanding of Li-N_2R. Previously, a bilayer structure was observed using in situ neutron reflectometry,[32] and $LiBF_4$ SEI was found to better limit proton transport to the Li surface using GIWAXS.[14] Without EtOH (Figure 4a), Li can react to form species like Li_3N, LiF, and other Li-organics from d_8-THF degradation products. Small amounts of LiD could be formed from d_8-THF degradation products. These species accumulate due to the passivation of Li, which leads to the formation of dendrites. In the presence of EtOH, additional species form, including LiH, LiEtO, and other Li-organics (Figure 4b-d). The protons from EtOH react with Li_3N or LiH to form NH_3 or H_2, leading to Li^+ dissolution. The inner layers formed in the presence of EtOH (both non-deuterated and deuterated) are an order of magnitude thinner, consistent with reduced Li species reacting EtOH.

When examining pathways in the cases with EtOH (Figure 4b-c), there is likely incorporation of boron into the organic outer layer as evident from neutron absorption. We also expect that proton-donor derived species would be incorporated along with solvent degradation products into the outer layer after continued cycling, though for the experiments here, the outer layer composition is largely dominated by the solvent.[26,31,56] The outer layer is highly porous and can be filled with electrolyte. It is within this SEI microenvironment that the desired path of NH_3 production takes place. However, we have also observed evidence for LiH formation that would likely serve as a pathway towards unfavored H_2 production or result from reaction of Li with formed H_2 via EtOH reduction at the working electrode.

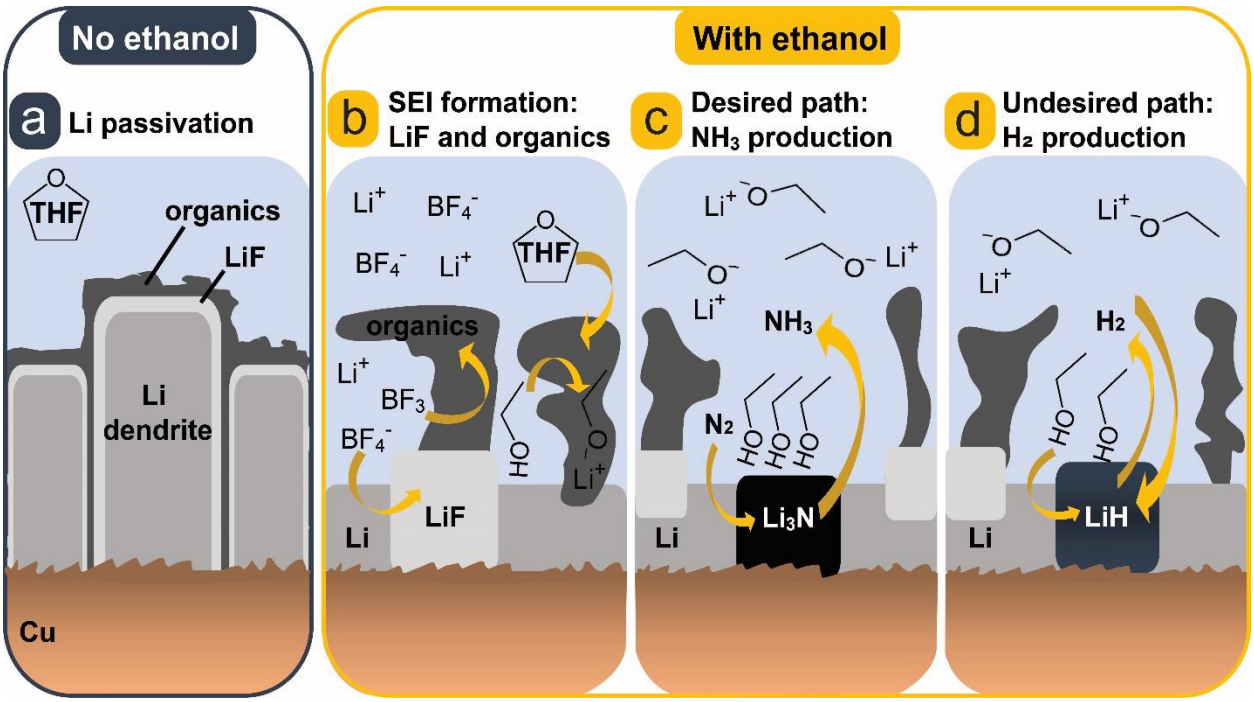

Figure 4. *Schematic of Li reaction scenarios during Li-N_2R (a) without EtOH and (b-d) with EtOH present, based on the interface structure and composition findings revealed in this study (a) Without EtOH, Li passivation occurs. (b) Li reacts to form the SEI, including LiF and organic species. (c) Desired Li reactivity towards NH_3. (d) Undesired reaction pathways towards H_2.*

Conclusion

In summary, we used a combination of electrochemical measurements and in situ neutron reflectometry to demonstrate how the SEI interfaces form and develop based on parameters such as current density and cycling versus sustaining current. We examined time-resolved SEI growth and source, dynamics, and fate of proton-containing species via isotope contrasting. Our results suggest that cycling at low current densities enables the formation of a robust SEI. Increasing current density leads to a thinner outer layer with a thicker inner layer, while sustaining current leads to the formation of more Li- and H-containing species, including LiH. Additionally, we identify boron in the SEI across these conditions. Time-resolved study of early SEI formation with a deuteration contrast series of proton donor and solvent indicated that proton donor influences inner layer composition, while the solvent influences the outer layer composition. Steady-state measurements showed that the experiment without EtOH leads to Li-containing species accumulation. These findings illustrate key aspects of the interfacial microenvironment that drives electrochemical NH_3 synthesis. Our results support rational, nanoscale design of the interfacial microenvironment via techniques including additive and artificial-SEI engineering. Further, these methods inform the *in situ* study of solid-liquid interfaces and proton dynamics for energy storage and sustainable

chemical syntheses with potential for adaptation to other applications, including energy conversion and water purification.

Acknowledgements

V.A.N., P.B., N.H.D., J.B.V.M., I.C., and T.F.J. acknowledge funding from the Villum Fonden (V-SUSTAIN grant 9455). V.A.N. was supported under the National Science Foundation Graduate Research Fellowship Program under grant no. DGE-1656518 and the Camille and Henry Dreyfus Foundation. S.W.L., A.C.N., W.A.T., and T.F.J. were supported by the U.S. Department of Energy, Office of Science, Office of Basic Energy Sciences, Chemical Sciences, Geosciences, and Biosciences Division, Catalysis Science Program through the SUNCAT Center for Interface Science and Catalysis. This research was performed at the Spallation Neutron Source, a Department of Energy (DOE) Office of Science User Facility operated by ORNL which is managed by UT-Battelle LLC for DOE under Contract DE-AC05-00OR22725. NMR measurements were supported by the NIH High End Instrumentation grant (1 S10 OD028697-01) and conducted at Stanford University. Part of this work was performed at the Stanford Nano Shared Facilities (SNSF), supported by the National Science Foundation under award ECCS-2026822. This research was pssxerformed in part at the nano@Stanford labs, which are supported by the National Science Foundation, part of the National Nanotechnology Coordinated Infrastructure under award ECCS-2026822. We thank Dr. Hanyu Wang, Professor Matteo Cargnello, and Dr. Eric McShane for their helpful conversations.

References

1. Stamenkovic, V. R., Strmcnik, D., Lopes, P. P. & Markovic, N. M. Energy and fuels from electrochemical interfaces. *Nat. Mater.* **16**, 57–69 (2017).
2. Butler, K. T., Sai Gautam, G. & Canepa, P. Designing interfaces in energy materials applications with first-principles calculations. *Npj Comput. Mater.* **5**, 19 (2019).
3. Srimuk, P., Su, X., Yoon, J., Aurbach, D. & Presser, V. Charge-transfer materials for electrochemical water desalination, ion separation and the recovery of elements. *Nat. Rev. Mater.* **5**, 517–538 (2020).
4. Candeago, R. *et al.* Unraveling the Role of Solvation and Ion Valency on Redox-Mediated Electrosorption through In Situ Neutron Reflectometry and Ab Initio Molecular Dynamics. *JACS Au* jacsau.3c00705 (2024) doi:10.1021/jacsau.3c00705.

5. Oyakhire, S. T. & Bent, S. F. Interfacial engineering of lithium metal anodes: what is left to uncover? *Energy Adv.* 10.1039.D3YA00470H (2024) doi:10.1039/D3YA00470H.
6. Lv, J. *et al.* Microenvironment Engineering for the Electrocatalytic CO_2 Reduction Reaction. *Angew. Chem. Int. Ed.* **61**, e202207252 (2022).
7. Steinmann, S. N. & Seh, Z. W. Understanding electrified interfaces. *Nat. Rev. Mater.* **6**, 289–291 (2021).
8. Guo, J. *et al.* Mass Transport Modifies the Interfacial Electrolyte to Influence Electrochemical Nitrate Reduction. *ACS Sustain. Chem. Eng.* **11**, 7882–7893 (2023).
9. Li, S. *et al.* Electrosynthesis of ammonia with high selectivity and high rates via engineering of the solid-electrolyte interphase. *Joule* **6**, 2083–2101 (2022).
10. Li, K. *et al.* Enhancement of lithium-mediated ammonia synthesis by addition of oxygen. *Science* **374**, 1593-1597 (2021).
11. Tao, M. *et al.* Quantifying the Evolution of Inactive Li/Lithium Hydride and Their Correlations in Rechargeable Anode-free Li Batteries. *Nano Lett.* **22**, 6775–6781 (2022).
12. Zachman, M. J., Tu, Z., Choudhury, S., Archer, L. A. & Kourkoutis, L. F. Cryo-STEM mapping of solid–liquid interfaces and dendrites in lithium-metal batteries. *Nature* **560**, 345–349 (2018).
13. Xu, G. *et al.* The Formation/Decomposition Equilibrium of LiH and its Contribution on Anode Failure in Practical Lithium Metal Batteries. *Angew. Chem. Int. Ed.* **60**, 7770–7776 (2021).
14. Deissler, N. H. *et al. Operando* investigations of the solid electrolyte interphase in the lithium mediated nitrogen reduction reaction. *Energy Environ. Sci.* 10.1039.D3EE04235A (2024) doi:10.1039/D3EE04235A.
15. Ovalle, V. J. & Waegele, M. M. Influence of pH and Proton Donor/Acceptor Identity on Electrocatalysis in Aqueous Media. *J. Phys. Chem. C* **125**, 18567–18578 (2021).
16. Padavala, S. K. M. & Stoerzinger, K. A. Role of Hydride Formation in Electrocatalysis for Sustainable Chemical Transformations. *ACS Catal.* **13**, 4544–4551 (2023).

17. Andersen, S. Z. *et al.* A rigorous electrochemical ammonia synthesis protocol with quantitative isotope measurements. *Nature* **570**, 504–508 (2019).
18. Fu, X. *et al.* Continuous-flow electrosynthesis of ammonia by nitrogen reduction and hydrogen oxidation. *Science* **379**, 707–712 (2023).
19. Li, S. *et al.* Long-term continuous ammonia electrosynthesis. *Nature* **629**, 92–97 (2024).
20. Fichter, Fr., Girard, P. & Erlenmeyer, H. Elektrolytische Bindung von komprimiertem Stickstoff bei gewöhnlicher Temperatur. *Helv. Chim. Acta* **13**, 1228–1236 (1930).
21. Tsuneto, A., Kudo, A. & Sakata, T. Efficient Electrochemical Reduction of N_2 to NH_3 Catalyzed by Lithium. *Chem. Lett.* **22**, 851–854 (1993).
22. Tsuneto, A., Kudo, A. & Sakata, T. Lithium-mediated electrochemical reduction of high pressure N2 to NH3. *J. Electroanal. Chem.* **367**, 183–188 (1994).
23. Lazouski, N., Schiffer, Z. J., Williams, K. & Manthiram, K. Understanding Continuous Lithium-Mediated Electrochemical Nitrogen Reduction. *Joule* **3**, 1127–1139 (2019).
24. Cai, X. *et al.* Lithium-mediated electrochemical nitrogen reduction: Mechanistic insights to enhance performance. *iScience* **24**, (2021).
25. Andersen, S. Z. *et al.* Increasing stability, efficiency, and fundamental understanding of lithium-mediated electrochemical nitrogen reduction. *Energy Environ. Sci.* **13**, 4291–4300 (2020).
26. Steinberg, K. *et al.* Imaging of nitrogen fixation at lithium solid electrolyte interphases via cryo-electron microscopy. *Nat. Energy* **8**, 138–148 (2022).
27. Aurbach, D. & Weissman, I. On the possibility of LiH formation on Li surfaces in wet electrolyte solutions. *Electrochem. Commun.* **1**, 324–331 (1999).
28. Lazouski, N. *et al.* Proton Donors Induce a Differential Transport Effect for Selectivity toward Ammonia in Lithium-Mediated Nitrogen Reduction. *ACS Catal.* **12**, 5197–5208 (2022).
29. Chang, W., Jain, A., Rezaie, F. & Manthiram, K. Lithium-mediated nitrogen reduction to ammonia via the catalytic solid–electrolyte interphase. *Nat. Catal.* (2024) doi:10.1038/s41929-024-01115-6.

30. Spry, M. *et al.* Water Increases the Faradaic Selectivity of Li-Mediated Nitrogen Reduction. *ACS Energy Lett.* **8**, 1230–1235 (2023).
31. McShane, E. J. *et al.* Quantifying Influence of the Solid-Electrolyte Interphase in Ammonia Electrosynthesis. *ACS Energy Lett.* **8**, 4024–4032 (2023).
32. Blair, S. J. *et al.* Combined, time-resolved, *in situ* neutron reflectometry and X-ray diffraction analysis of dynamic SEI formation during electrochemical N_2 reduction. *Energy Environ. Sci.* **16**, 3391–3406 (2023).
33. Du, H.-L. *et al.* Electroreduction of nitrogen with almost 100% current-to-ammonia efficiency. *Nature* **609**, 722–727 (2022).
34. Hobold, G. M., Wang, C., Steinberg, K., Li, Y. & Gallant, B. M. High lithium oxide prevalence in the lithium solid–electrolyte interphase for high Coulombic efficiency. *Nat. Energy* (2024) doi:10.1038/s41560-024-01494-x.
35. Browning, K. L. *et al.* The Study of the Binder Poly(acrylic acid) and Its Role in Concomitant Solid–Electrolyte Interphase Formation on Si Anodes. *ACS Appl. Mater. Interfaces* **12**, 10018–10030 (2020).
36. Browning, K. L. *et al. In Situ* Measurement of Buried Electrolyte–Electrode Interfaces for Solid State Batteries with Nanometer Level Precision. *ACS Energy Lett.* **8**, 1985–1991 (2023).
37. Penfold, J. & Thomas, R. K. The application of the specular reflection of neutrons to the study of surfaces and interfaces. *J. Phys. Condens. Matter* **2**, 1369–1412 (1990).
38. Blair, S. J. *et al.* Lithium-Mediated Electrochemical Nitrogen Reduction: Tracking Electrode–Electrolyte Interfaces via Time-Resolved Neutron Reflectometry. *ACS Energy Lett.* **7**, 1939–1946 (2022).
39. Ankner, J.F. *et al.* The SNS Liquids Reflectometer. *Neutron News* **19**, 14–16 (2008).
40. Kienzle, P. A. *et al.* Refl1D Reflectometry Software. (2017).
41. Maranville, B.B. *et al.* REFL1D. https://github.com/ reflectometry/refl1d.

42. Vrugt, J.A., Ter Braak, C.J.F., Diks, C.G.H., Robinson, B.A., & Hyman, J.M. Accelerating Markov Chain Monte Carlo Simulation by Differential Evolution with Self-Adaptive Randomized Subspace Sampling. *Int. J. Nonlinear Sci. Numer. Simul.* **10**, 273–290 (2009).
43. McShane, E. J. *et al.* A Versatile $Li_{0.5}FePO_4$ Reference Electrode for Nonaqueous Electrochemical Conversion Technologies. *ACS Energy Lett.* **8**, 230–235 (2023).
44. Kanamura, K., Tamura, H., Shiraishi, S. & Takehara, Z. XPS Analysis of Lithium Surfaces Following Immersion in Various Solvents Containing LiBF4. *J. Electrochem. Soc.* **142**, 340–347 (1995).
45. Zhang, S. S., Xu, K. & Jow, T. R. Study of LiBF4 as an Electrolyte Salt for a Li-Ion Battery. *J. Electrochem. Soc.*
46. Xu, K. Nonaqueous Liquid Electrolytes for Lithium-Based Rechargeable Batteries. *Chem. Rev.* **104**, 4303–4418 (2004).
47. Lazouski, N. *et al.* Proton Donors Induce a Differential Transport Effect for Selectivity toward Ammonia in Lithium-Mediated Nitrogen Reduction. *ACS Catal.* 5197–5208 (2022) doi:10.1021/acscatal.2c00389.
48. An, S. J. *et al.* The state of understanding of the lithium-ion-battery graphite solid electrolyte interphase (SEI) and its relationship to formation cycling. *Carbon* **105**, 52–76 (2016).
49. Ramasubramanian, A. *et al.* Stability of Solid-Electrolyte Interphase (SEI) on the Lithium Metal Surface in Lithium Metal Batteries (LMBs). *ACS Appl. Energy Mater.* **3**, 10560–10567 (2020).
50. Deshpande, R. D. & Bernardi, D. M. Modeling Solid-Electrolyte Interphase (SEI) Fracture: Coupled Mechanical/Chemical Degradation of the Lithium Ion Battery. *J. Electrochem. Soc.* **164**, A461–A474 (2017).
51. Schwalbe, J. A. *et al.* A Combined Theory-Experiment Analysis of the Surface Species in Lithium-Mediated NH_3 Electrosynthesis. *ChemElectroChem* **7**, 1542–1549 (2020).

52. Aoki, Y. *et al.* Effective Approach by Computational Chemical Prediction and Experimental Verification to Elucidate SEI Formation Mechanism in $LiPF_6$ -, LiFSI-, and $LiBF_4$ -Containing Electrolyte Solutions. *J. Phys. Chem. C* **127**, 69–77 (2023).
53. Parimalam, B. S. & Lucht, B. L. Reduction Reactions of Electrolyte Salts for Lithium Ion Batteries: $LiPF_6$, $LiBF_4$, LiDFOB, LiBOB, and LiTFSI. *J. Electrochem. Soc.* **165**, A251–A255 (2018).
54. Andersson, A. M., Herstedt, M., Bishop, A. G. & Edström, K. The influence of lithium salt on the interfacial reactions controlling the thermal stability of graphite anodes. *Electrochimica Acta* **47**, 1885–1898 (2002).
55. Magnussen, O. M. *et al. In Situ* and *Operando* X-ray Scattering Methods in Electrochemistry and Electrocatalysis. *Chem. Rev.* **124**, 629–721 (2024).
56. Bjarke Valbæk Mygind, J. *et al.* Is Ethanol Essential for the Lithium-Mediated Nitrogen Reduction Reaction? *ChemSusChem* **16**, e202301011 (2023).
57. Zhuang, G. R., Wang, K., Chen, Y. & Ross, P. N. Study of the reactions of Li with tetrahydrofuran and propylene carbonate by photoemission spectroscopy. *J. Vac. Sci. Technol. Vac. Surf. Films* **16**, 3041–3045 (1998).
58. Sažinas, R. *et al.* Towards understanding of electrolyte degradation in lithium-mediated non-aqueous electrochemical ammonia synthesis with gas chromatography-mass spectrometry. *RSC Adv.* **11**, 31487–31498 (2021).